Radio-Based Simultaneous Localization and Mapping Exploiting Low-Complexity Angular Information

Benedikt J. Müller, Armin Dammann, Martin Schmidhammer, Michael Walter, Siwei Zhang, Christian Gentner
Institute of Communications and Navigation, *German Aerospace Center (DLR)*, 82234 Weßling, Germany
{benedikt.mueller, armin.dammann, martin.schmidhammer, m.walter, siwei.zhang, christian.gentner}@dlr.de

***Abstract*—Multipath propagation can be exploited as a source of geometric information for radio-based localization and mapping. This paper investigates a multipath-assisted approach for jointly estimating the position of a moving receiver and the reflection points in its surroundings. Building on previous work, we compare low-complexity angular information from a two-antenna receiver array using phase difference of arrival (PDoA), Doppler, and their combination. In realistic scenarios, we also considered snapshot-based initialization, multi-hypothesis tracking, and simultaneous self-localization. Since the approach requires only a simple ranging protocol and two receiver antennas, it is suitable for low-cost radio platforms such as ultra-wideband systems.**

Simulation results demonstrate that reflection points (RPs) can be tracked using distance measurements combined with angular information from PDoA, Doppler, or both. The results show that estimation performance depends strongly on the orientation of the measurement symmetry axis. Tracking is more stable and accurate when this axis is perpendicular to the propagation path. In realistic scenarios, the combination of distance, Doppler, and PDoA measurements with perpendicular symmetry axes provided the most robust tracking performance and also resolved initialization ambiguities quickly. The results highlight the potential of direct RP estimation for mapping unknown, non-planar, and irregular environments without relying on static virtual transmitters or straight-wall models.

***Index Terms*—Multipath-assisted localization, radio-based SLAM, reflection point tracking, phase difference of arrival, Doppler, UWB.**

I. Introduction

Safe and effective navigation of autonomous mobile systems requires both accurate localization and robust environmental awareness [1]. Reliable localization and environmental perception, however, becomes particularly challenging in visually degraded and global navigation satellite system (GNSS)-denied environments, such as collapsed structures, underground facilities, or cluttered indoor areas. In such scenarios, radio-based approaches have emerged as a compelling alternative, as radio signals can penetrate visually obscured environments and inherently encode information about the surrounding scene through their propagation characteristics.

In indoor and obstructed radio environments, the received signal typically consists of several propagation paths rather than only a direct line-of-sight (LoS) component. Reflections, diffraction, and scattering at surrounding objects generate delayed signal components, referred to as multipath components (MPCs). While conventional positioning methods often treat these components as impairments, multipath-assisted positioning exploits them as additional measurements, containing geometric information. A widely used formulation represents reflected MPCs as direct paths emitted by virtual transmitters (VTs), whose locations are estimated jointly with the mobile receiver state [2]–[4]. These conventional VT-based methods assume that the reflecting surfaces can be represented by static VTs. This representation is well suited for planar walls, but it becomes restrictive when the environment contains curved, irregular, or cluttered boundaries. Recent work has therefore started to address more general boundary shapes [5]–[7]. Other studies have investigated the use of angular information from antenna arrays to improve localization and mapping performance [8]. These developments indicate that richer measurement models are required when radio-based mapping is applied, especially outside simplified straight-wall scenarios.

In [7], a multipath-assisted simultaneous localization and mapping (SLAM) method was proposed that directly estimates physical reflection points (RPs) instead of relying on VTs. By combining distance and relative Doppler measurements, the method was shown to localize a moving receiver and map first-order RPs on walls with arbitrary shapes, including convex and concave geometries. The present work extends this idea by studying how different sources of limited angular information affect the estimation of RPs. In particular, we compare Doppler-based measurements with phase difference of arrival (PDoA)-based measurements obtained from a two-antenna receiver array, and we analyze how both measurement types can be combined. We focus here on low-complexity angular information, excluding large antenna arrays [6]. The goal is to gain in-depth understanding about the role of ambiguous angular information for RP-based radio SLAM (RP-SLAM) problems.

The key observation in this paper is that both Doppler and PDoA measurements provide ambiguous angular information with a characteristic symmetry axis. For Doppler measurements with a static transmitter (Tx), this axis is determined by the velocity direction of the mobile receiver. For PDoA measurements, it can be changed by rotating the mounting angle of the receiver antenna array. This flexibility makes the relative orientation between the measurement symmetry axis and the propagation path an important design parameter. We therefore investigate how this orientation influences the tracking accuracy of RPs and whether unfavorable measurement geometries can be compensated by adapting the assumed measurement noise.

The proposed approach is evaluated first in simplified simulation scenarios with different measurement configurations. These simulations isolate the influence of the measurement symmetry axis and show that configurations with a symmetry axis perpendicular to the propagation path provide significantly better estimation performance than aligned configurations. Second, we consider more realistic scenarios including snapshot-based initialization, multi-hypothesis tracking (MHT), and simultaneous localization of the mobile receiver.

The results show that combining distance, Doppler, and PDoA measurements with perpendicular symmetry axes provides the most robust tracking behavior. This configuration improves stability in challenging trajectories and resolves initialization ambiguities more reliably, while increased noise values for unfavorable symmetry-axis orientations can partly compensate for adverse geometric conditions. Overall, the paper demonstrates that the combination of Doppler and two-antenna PDoA information is a practical extension of the Doppler-only RP-SLAM method, while retaining compatibility with low-cost ultra-wideband (UWB)-based platforms. Further it builds valuable intuition about angular information in RP-SLAM for challenging and realistic indoor environments.

II. Method

In this chapter we first present the general system description and then define the corresponding state model. Next, the measurement model is defined, where we especially discuss the angular measurements. At the end of the chapter, we introduce the estimation methods used during this work.

A. State model

Following [7], we consider a planar environment with known static anchor locations and unknown dynamic mobile positions. The propagation environment further contains walls with unknown geometry, which induce signal reflections between mobile and anchor nodes. Since we want to use MPC information in this work and the corresponding RPs are unknown, we have to estimate them jointly with the mobile, leading to a SLAM problem. Only first-order wall interactions are modeled, i.e. for a given LoS Tx–receiver (Rx) pair, each wall can generate one RP and one associated MPC. Using first-order reflections is motivated by the fact that such reflections typically constitute the dominant reflected components that can be exploited reliably [9]. Higher-order reflections with sufficient power can be distinguished, as they do not form stable RP tracks within the employed SLAM formulation.

We denote the set of all mobiles, anchors and reflection points as $\mathcal{M}$, $\mathcal{A}$ and $\mathcal{R}$. For each mobile, anchor, or RP $i \in \mathcal{M} \cup \mathcal{A} \cup \mathcal{R}$, we define the state $\boldsymbol{x}_i = [x_i, \dot{x}_i, y_i, \dot{y}_i]^\top$, which consists of the position $\boldsymbol{p}_i = [x_i, y_i]^\top$ and velocity $\dot{\boldsymbol{p}}_i = [\dot{x}_i, \dot{y}_i]^\top$. Temporal derivatives are indicated by a dot, throughout this work. Note that every RP $r \in \mathcal{R}$ corresponds to a signal propagation between nodes i and j, but depending on the wall geometry a single node pair (i, j) may generate multiple RPs along different wall segments. Since only the locations of the stationary anchors are known, we define the full state vector $\boldsymbol{s}$, composed of all unknowns, as

$$\boldsymbol{s} = \left[\left(\boldsymbol{x}_i^\top\right)_{i\in\mathcal{M}\cup\mathcal{R}}\right]^\top . \tag{1}$$

Let t_k denote the time of snapshot $k \in \mathbb{N}$, $\Delta t_k = t_{k+1} - t_k$ the time increment to the next snapshot, and $\boldsymbol{s}_k$ the corresponding state vector at this time step. For the state transition we use the constant velocity model [10], with

$$\boldsymbol{s}_{k+1} = \boldsymbol{F}_k\, \boldsymbol{s}_k + \boldsymbol{\eta}_k\,, \quad \boldsymbol{\eta}_k \sim \mathcal{N}\left(0, \boldsymbol{Q}_k\right) . \tag{2}$$

The state-transition matrix F_k is given by

$$\boldsymbol{F}_i(\Delta t) = \begin{bmatrix} 1 & \Delta t & 0 & 0 \\ 0 & 1 & 0 & 0 \\ 0 & 0 & 1 & \Delta t \\ 0 & 0 & 0 & 1 \end{bmatrix} , \quad i \in \mathcal{M}\cup\mathcal{R}\,, \tag{3}$$

$$\boldsymbol{F}_k = \operatorname{blkdiag}\big(\left(\boldsymbol{F}_i\left(\Delta t_k\right)\right)_{i\in\mathcal{M}\cup\mathcal{R}}\big)\ , \quad k \in \mathbb{N}\,. \tag{4}$$

and the corresponding process-noise covariance Q_k is

$$\boldsymbol{Q}_i(\Delta t) = \sigma^2_{\mathrm{m/r}} \begin{bmatrix} \frac{\Delta t^3}{3} & \frac{\Delta t^2}{2} & 0 & 0 \\ \frac{\Delta t^2}{2} & \Delta t & 0 & 0 \\ 0 & 0 & \frac{\Delta t^3}{3} & \frac{\Delta t^2}{2} \\ 0 & 0 & \frac{\Delta t^2}{2} & \Delta t \end{bmatrix} , \quad i \in \mathcal{M}\cup\mathcal{R}\,, \tag{5}$$

$$\boldsymbol{Q}_k = \operatorname{blkdiag}\big(\left(\boldsymbol{Q}_i\left(\Delta t_k\right)\right)_{i\in\mathcal{M}\cup\mathcal{R}}\big)\ , \quad k \in \mathbb{N}\,, \tag{6}$$

where the process noise variances of mobiles and RPs are σ^2_{m} and σ^2_{r}, respectively.

B. Measurement model

In this work we focus on three different types of measurements at the mobile: time of flight (ToF) which contains distance information, PDoA and Doppler information which both contain angular information. Each propagation path between node i and j, with $i, j \in \mathcal{M}\cup\mathcal{A}$, can potentially generate these measurements, be it the LoS path ij or an MPC irj connecting the two nodes over RP $r \in \mathcal{R}$. Therefore, we can define the first measurement, which corresponds to the distance d, as

$$d_{kl} = \|\boldsymbol{p}_k - \boldsymbol{p}_l\|\ , \quad d_{irj} = d_{ir} + d_{rj}\,, \tag{7}$$

where we defined the general distance d_{kl} between two points $k, l \in \mathcal{M}\cup\mathcal{A}\cup\mathcal{R}$ including the LoS distances, as well as the MPC distances d_{irj}.

We adopt the Doppler measurement definition from [7]. With a suitable tracking algorithm for the distance measurement, the distance change rate $\dot{d}$ can be used to derive the delay change rate $\dot{\tau}$, which is proportional to the Doppler value v. Consequently, in contrast to the relative Doppler-observation setting discussed in [7], the delay change rate provides access not only to relative Doppler information but to absolute Doppler information, provided that the measurement frequency is sufficiently high. Therefore, we define the Doppler measurement v_{kl}, $k, l \in \mathcal{A}\cup\mathcal{M}\cup\mathcal{R}$, as the projected velocity onto the propagation path

$$v_{kl} = \frac{\boldsymbol{p}_l - \boldsymbol{p}_k}{\|\boldsymbol{p}_l - \boldsymbol{p}_k\|} \cdot \left(\dot{\boldsymbol{p}}_k - \dot{\boldsymbol{p}}_l\right) . \tag{8}$$

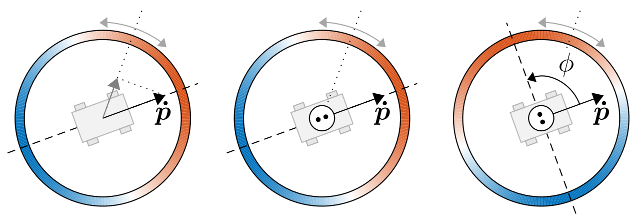

(a) Doppler v (b) PDoA $\theta_{\|}$ (c) PDoA $\theta_{\perp}$

Fig. 1. Different angular measurements schematically. The gradient shows the measured values, depending on the angle of the incoming wave's propagation path (dotted). In (a) the Doppler measurement is illustrated. It is essentially a projection of the velocity vector onto the propagation path, if the anchor is static. In (b) and (c), we see the values of a PDoA measurement from $-\pi$ (dark blue) to π (dark red), for a mounting angle of the two-antenna array towards the mobile (light gray) of $\phi = 0$ and $\phi = \frac{\pi}{2}$, respectively. The symmetry axis (dashed) of each of the different measurements is highlighting the occurring measurement ambiguities on both sides of the axis.

For an MPC of a first-order reflection consists of two components (8). Thus, for RP $r \in \mathcal{R}$ and nodes $i, j \in \mathcal{M} \cup \mathcal{A}$ the Doppler measurement is the sum

$$\begin{aligned} v_{irj} &= v_{ir} + v_{rj} \\ &= \frac{(\boldsymbol{p}_r - \boldsymbol{p}_i)}{d_{ir}} \cdot (\dot{\boldsymbol{p}}_i - \dot{\boldsymbol{p}}_r) + \frac{(\boldsymbol{p}_j - \boldsymbol{p}_r)}{d_{jr}} \cdot (\dot{\boldsymbol{p}}_r - \dot{\boldsymbol{p}}_j) \\ &= \frac{(\boldsymbol{p}_r - \boldsymbol{p}_i) \cdot \dot{\boldsymbol{p}}_i}{d_{ir}} + \frac{(\boldsymbol{p}_r - \boldsymbol{p}_j) \cdot \dot{\boldsymbol{p}}_j}{d_{jr}} , \end{aligned} \tag{9}$$

where the contributions of the RP movement $\dot{\boldsymbol{p}}_r$ vanish, because the wall itself is static and thus $\dot{\boldsymbol{p}}_r$ must be tangential to the wall and additionally the angle of incidence equals angle of reflection. Note that for a mobile $i \in \mathcal{M}$ and a static anchor $j \in \mathcal{A}$ the latter part in (9) vanishes due to $\dot{\boldsymbol{p}}_j = 0$.

We define the PDoA θ at a two-antenna array as the third measurement. All nodes may have either one antenna or a two antennas with antenna spacing d_{ant} and orientation ϕ to the moving direction, see Fig. 1. In general the position of the mobile and anchors is defined at the position of their antenna. However, in the case of a two-antenna array, we do not model the antenna positions separately in the state vector but assume that d_{ant} is small compared to the system scale. The PDoA measurement is essentially a difference in phase between the two antennas due to the signal arriving at the antennas at different time points. Mathematically we describe this measurement for a node $i \in \mathcal{M} \cup \mathcal{A}$ with a two-antenna array and an incoming ray from either another node (LoS) or an RP (MPC) $k \in \mathcal{M} \cup \mathcal{A} \cup \mathcal{R}$ as

$$\tilde{\theta}_{ik} = \frac{2\pi\, d_{\text{ant}}}{\lambda} \left(\boldsymbol{R}_\phi \cdot \frac{\dot{\boldsymbol{p}}_i}{\|\dot{\boldsymbol{p}}_i\|} \right) \cdot \frac{\boldsymbol{p}_j - \boldsymbol{p}_i}{\|\boldsymbol{p}_i - \boldsymbol{p}_j\|} , \tag{10}$$

$$\theta_{ik} = \operatorname{mod}\left(\tilde{\theta}_{ik} + \pi,\, 2\pi\right) - \pi , \tag{11}$$

with the wavelength λ and the rotation matrix $\boldsymbol{R}_\phi$ which rotates the normalized velocity vector by ϕ in order to derive the orientation of the antenna array. Note that for $d_{\text{ant}} \leq \lambda/2$ the mapping in (11) has no effect. If we additionally choose an array orientation along the velocity vector, i.e. $\phi = 0$, then the PDoA information is closely related to the Doppler information received at node i, see (8) and (9), from a static Tx node j and only differs by a constant factor and the normalization of the velocity vector $\dot{\boldsymbol{p}}_i$. The similarity exists for all paths, LoS and MPC, between node i and j. The close relation results in equivalent symmetry axes between the two measurements, see Fig. 1, and is later on visible in the performance comparisons.

In this work we will investigate the influence of different measurements on the estimation performance. Therefore, the composition of the measurement function $\boldsymbol{H}$ is different for different scenario configurations, we can write the full measurement function as

$$\begin{aligned} \boldsymbol{H}(\boldsymbol{s}) :=& \boldsymbol{H}\left(\boldsymbol{s}; (\boldsymbol{x}_i)_{i \in \mathcal{A}}, \phi, d_{\text{ant}}\right) \\ =& \Big[(d_{ij}, v_{ij}, \theta_{ij})_{i \in \mathcal{M},\, j \in \mathcal{A} \cup \mathcal{M},\, r \in \mathcal{R},\, i<j \text{ if } i,j \in \mathcal{M}} , \\ & (d_{irj}, v_{irj}, \theta_{ir})_{i \in \mathcal{M},\, j \in \mathcal{A} \cup \mathcal{M},\, r \in \mathcal{R},\, i<j \text{ if } i,j \in \mathcal{M}} \Big]^\top . \end{aligned} \tag{12}$$

Note that a specific scenario may use only a subset of the full measurement vector H.

Next we define the model to calculate a measurement z_k at time t_k as

$$\boldsymbol{z}_k = \boldsymbol{H}(\boldsymbol{s}_k) + \boldsymbol{\mu}_k , \quad \boldsymbol{\mu}_k \sim \mathcal{N}(0, \boldsymbol{\Sigma}) , \tag{13}$$

with the measurement covariance matrix $\boldsymbol{\Sigma}$,

$$\begin{aligned} \boldsymbol{\Sigma} = \operatorname{diag}\Big(& (\sigma^2_{\text{dm}}, \sigma^2_{\text{vm}}, \sigma^2_{\theta\text{m}})_{i \in \mathcal{M},\, j \in \mathcal{A} \cup \mathcal{M},\, i<j \text{ if } j \in \mathcal{M}} , \\ & (\sigma^2_{\text{dr}}, \sigma^2_{\text{vr}}, \sigma^2_{\theta\text{r}})_{i \in \mathcal{M},\, r \in \mathcal{R},\, j \in \mathcal{A} \cup \mathcal{M},\, i<j \text{ if } j \in \mathcal{M}} \Big) , \end{aligned} \tag{14}$$

with the variances of the different measurements $\sigma^2_{\text{dm}}, \sigma^2_{\text{vm}}, \sigma^2_{\theta\text{m}}, \sigma^2_{\text{dr}}, \sigma^2_{\text{vr}}, \sigma^2_{\theta\text{r}}$ for mobiles and RPs respectively.

C. Estimator

We use an extended Kalman filter (EKF) as estimator, following the formulation in [7], [11]. The filter first predicts the next state $\boldsymbol{s}_{k+1}$ and covariance $\boldsymbol{P}_{k+1}$ using (2), then compares the predicted measurements from (13) with the data and updates the prediction accordingly.

For the initialization of the mobile state $\boldsymbol{p}_i$, $i \in \mathcal{M}$, we use the true state perturbed by process noise, in order to simulate a scenario where the mobiles enter from a known environment an unknown environment. When a new RP is detected, the full state vector and the matrices $\boldsymbol{s}, \boldsymbol{P}, \boldsymbol{F}, \boldsymbol{Q}, \boldsymbol{H}, \boldsymbol{\Sigma}$ are expanded and the initial velocity is set to zero. The initialization of RPs position in the tracking filter is done via one of two different methods. The first method initializes the RP position in a genie-aided fashion by perturbing the true RP position with Gaussian noise of standard deviation σ_{ini}. It is used in simplified scenarios. The second method is applicable for more realistic scenarios and consists of two steps, first we calculate for the current snapshot measurements likely positions of the new RP. The likelihood l_k and the log-likelihood L_k of a measurement $\boldsymbol{z}_k$ given a state $\boldsymbol{s}_k$ at snapshot k can be computed by using the Mahalanobis distance [12],

$$d_{\mathrm{m},k} = \sqrt{\left(\boldsymbol{H}(\boldsymbol{s}) - \boldsymbol{z}_k\right)^\top \boldsymbol{\Sigma}^{-1} \left(\boldsymbol{H}(\boldsymbol{s}) - \boldsymbol{z}_k\right)}, \tag{15}$$

$$l_k = p(\boldsymbol{z}_k|\boldsymbol{s}_k) = \frac{1}{\sqrt{|\det(2\pi\boldsymbol{\Sigma})|}} \exp\left(-\frac{d_{\mathrm{m},k}^2}{2}\right), \tag{16}$$

$$L_k = \ln(l_k) = -\frac{1}{2} d_{\mathrm{m},k}^2 + \text{const.}, \tag{17}$$

where $p(\cdot\,|\,\cdot)$ denotes a probability, not a position. Depending on the measurement configuration, these snapshot measurements may be ambiguous and thus return multiple, equally likely, RP positions, called hypothesis. Then in a second step we do what is called MHT in literature [13], [14]. If there is only one hypothesis for the new RP, we add it to the estimated state vector and continue tracking. If there are multiple hypothesis, we bifurcate the filter, i.e. create parallel filter instances, one for each initial position hypothesis. These parallel filters are then kept for the following measurements and the likelihoods are calculated after each time-step according to (17). We can calculate the accumulated log-likelihood, $\tilde{L}_k = \tilde{L}_{k-1} + L_k - \text{const.}$, which defines the combined likelihood of all measurements up to this point, with $\tilde{L}_0 = 0$. We prune filter instances I whose likelihood relative to the currently best filter instance J (highest accumulated likelihood of all instances) falls below a threshold $\gamma_L > \tilde{L}_k^I - \tilde{L}_k^J$. We merge two filters if their state estimates are sufficiently close compared to their combined uncertainty. This is tested using the squared Mahalanobis distance and a 95 % threshold, $(\boldsymbol{s}^I - \boldsymbol{s}^J)^\top (\boldsymbol{P}^I/2 + \boldsymbol{P}^J/2)^{-1} (\boldsymbol{s}^I - \boldsymbol{s}^J) \leq \chi^2_{0.95}$, [12]. Ideally merging and pruning lead to the convergence towards one filter instance which is tracking the true state.

Upon the termination of an RP, due to the wall geometry and the current mobile position, the state vector and the matrices are reduced accordingly.

III. Simulation Environment

As a simulation setup we chose, similar to [7] a certain mobile m $\in \mathcal{M}$, two static anchors and a wall with different shapes. We chose several different variations within the above setup in order to compare the different measurements, introduced in section II-B, in their performance on estimating RP and or mobile positions. As a first step, we varied the measurement configuration across simulations. The distance measurements were used in all simulations, the angular measurements were varied in using Doppler or PDoA, the mounting angle $\phi \in \{0, \frac{\pi}{2}\}$ of the two-antenna array and the measurement uncertainty $\sigma_{\theta\mathrm{m/r}} \in \{0.35, \frac{\pi}{2}\}$, where the value $0.35\,\mathrm{rad} = 20°$ was conservatively taken from [15], [16]. Second, we varied the orientation of the trajectory with respect to the wall. As an initial mobile state we chose $\boldsymbol{x}_\mathrm{m} \in \{[-10\,\mathrm{m}, 1\,\mathrm{m/s}, 0, 0]^\top, [0, 0, -15\,\mathrm{m}, 1\,\mathrm{m/s}]^\top\}$, i.e. one initial trajectory parallel and one perpendicular to the wall (see also Fig. 2). Further we chose a low process noise of $\sigma_\mathrm{m} = 0.1\,\mathrm{m/s}^{3/2}$ for the mobile, such that the generated trajectory roughly keeps the direction of the initial state during the simulation time.

Finally, we varied the initialization method and estimation of the mobile: For a set of scenarios we used simplified conditions, known mobile trajectory and simple genie-aided RP initialization. For a similar set of scenarios we later simulated realistic conditions, with an unknown mobile trajectory and snapshot based initialization of an MHT.

We try to reduce model mismatch in order to have more clear results. Therefore, we use the same parameters for generation of the trajectory and estimation of the mobile state, as well as the same measurement parameters for estimation as used for generating the measurements. Parameters that are fixed throughout this work are, $\sigma_\mathrm{r} = 1.1805\,\mathrm{m/s}^{3/2}$ which is chosen higher than σ_m, since we know less about the dynamic of the RP. The measurement parameters are adapted from [7], $d_\mathrm{ant} \leq \lambda/2$, $\sigma_\mathrm{dm} = 0.1\,\mathrm{m}, \sigma_\mathrm{dr} = 0.3\,\mathrm{m}, \sigma_\mathrm{vm} = \sigma_\mathrm{vr} = 0.5\,\mathrm{m/s}$. For the estimation model we use as above mentioned different values for $\sigma_{\theta\mathrm{m/r}}$, depending on the scenario, but for generation of the measurements in the simulation we use $\sigma_{\theta\mathrm{m/r}} = 0.35\,\mathrm{rad}$ in all cases. For the perturbation of the initial RP position in the simplified scenario's genie-aided initialization, we used $\sigma_\mathrm{ini} = 2\,\mathrm{m}$. For the pruning threshold of the MHT we use $\gamma_L = 10$. In all simulations we used $\Delta t = 0.1\,\mathrm{s}$ and $k_\mathrm{max} = 200$ time steps.

IV. Results

In this chapter we will first discuss representative scenarios. After that, we will analyze a simplified quantitative scenario to isolate trends and understand effects. At the end, we test the feasibility of our algorithm in more realistic scenarios.

A. Representative scenarios

In Fig. 2, three representative scenarios with PDoA measurements are shown. Fig. 2 (a) shows a trajectory parallel to the wall with an array orientation of $\phi = 0$, (b) shows a similar track with $\phi = \frac{\pi}{2}$. In Fig. 2 (c) we see a trajectory perpendicular to the wall with mounting angle $\phi = \frac{\pi}{2}$.

We can see in (a), that if the track is parallel to the wall and the mounting angle is $\phi = 0$, the RPs can be tracked well.

For a similar trajectory and a different array orientation $\phi = \frac{\pi}{2}$, (b), the RP estimate drifts away from the wall. Further, the mobile estimate can also be degraded, if the RP estimate is far away from its true position, since the estimation of the two is combined here in a SLAM problem. The estimate degradation can be explained by noticing that here the symmetry axis of the measurement, see Fig. 1, points towards the wall and thus towards the RPs. When the symmetry axis is close to an RP, the estimator gets ambiguous measurement information, not knowing on which side the RP lies. If an RP is estimated on the wrong side of the symmetry axis, the estimator may lock onto this erroneous solution. As the symmetry axis turns away from the true RP position due to mobile motion or wall curvature, subsequent ambiguous measurements tend to keep the estimate on the wrong side. Consequently, the RP estimate drifts away from

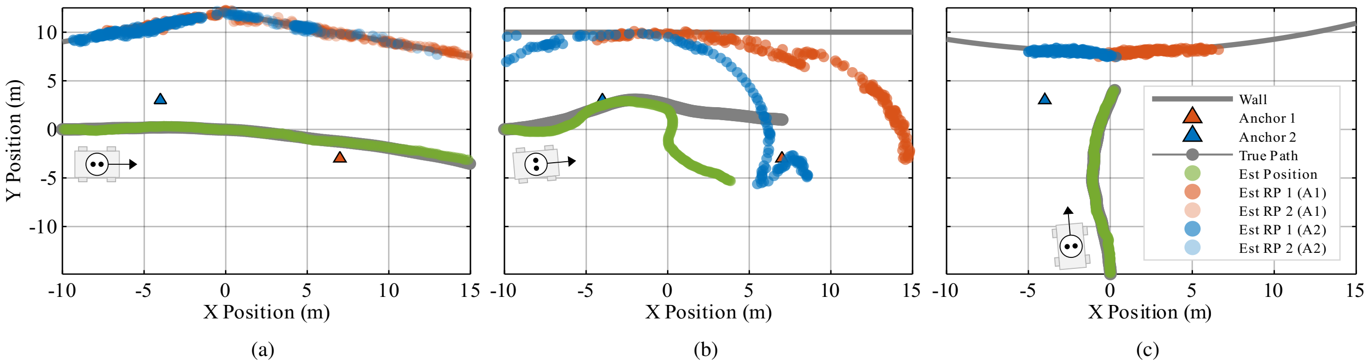

Fig. 2. Individual simulation runs for the proposed RP-SLAM method. In the shown simulations we used distance and PDoA measurements. We varied the mounting angle of the two-antenna array, $\phi = 0$ ($\theta_{\|}$) in (a) and $\phi = \frac{\pi}{2}$ ($\theta_{\perp}$) in (b) and (c). In (c) we also changed the initial conditions of the mobile such that the trajectory is perpendicular to the wall.

the wall. This behavior can be interpreted as the symmetry axis pushing the RP estimate away from the wall. The underlying cause is the increased effective PDoA measurement noise of a linear antenna array when the symmetry axis is approximately aligned with the propagation path. Equivalently, the estimator assigns too much confidence to an ambiguous measurement when the two snapshot solutions lie close to each other. The well-established reduction in near-endfire angular resolution [17] may further contribute to estimator overconfidence, but is not treated separately here. Notably the RPs drift away on an ellipse shape, which indicates that the distance measurements are still trustworthy and just the angular information from the PDoA measurement is misleading. The ellipse shape is dominant here, because the distance measurements restricts the possible first-order RPs onto an ellipse with sender and receiver as focal points.

Finally turning the track orientation in Fig. 2 (c), we see, that the same configuration as used in (b), is now able to sufficiently track the RPs, which solidifies the symmetry axis argument above. Further we can observe that in the case of the track being perpendicular to the wall, the RPs move a lot less on the wall even though the tracks have similar length. The reduced RP movement indicates that if the goal is to map a wall, it is best to move along the wall in order to have the moving RPs cover as much of the wall as possible over time.

B. Quantitative evaluation of simplified scenarios

After the qualitative discussion of representative simulation runs, we now use Monte Carlo (MC) simulations to quantify relevant trends and gain further insight from a broader range of scenarios and their statistical evaluation. Therefore, we simulated each scenario 10^4 times with a different randomly generated trajectory for each run. As wall shapes, we used the same geometries as in [7], equally distributed among all runs.

First, we look into the simplified scenario, with the mobile track known, in order to observe the effects of the different measurement configurations more isolated and thus more clearly. We assume, that the RPs can be initialized with a perturbed true position. Therefore, in this simplified scenario, the estimation is restricted on tracking the RPs and thus mapping the wall. The results of the different measurement configurations are shown in Fig. 3.

The first four configurations use only PDoA, as angular measurement (distance measurement is used in all configurations). Here we can see that also for many MC simulation runs, the two above results hold: One, if the symmetry axis of the PDoA measurements is aligned with the wall, i.e. $\theta_{\|}$ for the case of a trajectory parallel to the wall, and $\theta_{\perp}$ for perpendicular trajectory, the RPs can be tracked. And two, if the symmetry axis points towards the wall and thus along the propagation path, the RPs cannot be tracked. The unsuccessful tracking can be seen especially at the high median and 95th percentile position root mean square error (RMSE) values, since they are so high, that for the system dimensions used here, they imply that the RP estimates are not in the vicinity of the walls. Further we can observe that estimators with larger $\sigma_{\theta\mathrm{r}}$, $\theta_{\perp\mathrm{u}}$ and $\theta_{\|\mathrm{u}}$, produces a higher error, compared to $\theta_{\perp}$ and $\theta_{\|}$, if the symmetry axis is aligned to the wall. The change in performance can be explained by the mismatch in the measurement model, since the true measurement uncertainty used for generating the measurements is lower. This effect is inverted, if the symmetry axis is perpendicular to the wall, because than the effective measurement noise is as discussed above actually higher than the one used to generate the measurements. Therefore, $\theta_{\perp\mathrm{u}}$ and $\theta_{\|\mathrm{u}}$ measurements perform better here compared to their counterparts $\theta_{\perp}$ and $\theta_{\|}$, even though the values still suggest, that the estimated RPs drift away from the wall and are thus not successfully tracked, in many of the MC runs.

These effects can also be seen, when using only the Doppler measurement v, which has the same symmetry axis and simulation behaviour as $\theta_{\|}$. However, v performs worse than $\theta_{\|}$, if the path is parallel to the wall, because the noise used to generate the measurements is different. The performance difference has to be treated with caution, since the noise values for Doppler were estimated in [7] for 3.9 GHz UWB systems and the actual noise value of the Doppler measurement depend also on e.g. the measurement frequency. In the case of a path perpendicular to the wall, the values are similar to $\theta_{\|}$, since

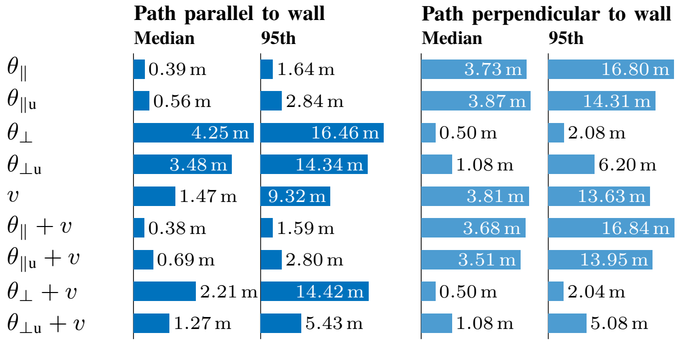

Fig. 3. Results of MC simulations in a simplified scenario, with known mobile position and genie-aided RP initialization. On the left for trajectories parallel and on the right perpendicular to the wall. Simulated PDoA configurations were $\phi = 0$ or $\phi = \frac{\pi}{2}$ (index $\|$ or $\perp$) and $\sigma_{\theta\mathrm{r}} = 0.35$ (no index) or $\sigma_{\theta\mathrm{r}} = \frac{\pi}{2}$ (index u). Other simulated angular measurement configurations are Doppler v and combinations of v with one of the PDoA variants. Note that the delay measurement was additionally used in all of the cases. The values correspond to specific quantiles of the RMSE distribution, with the bars normalized per column.

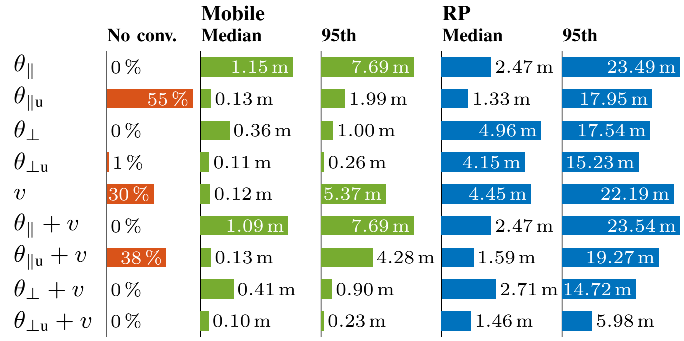

Fig. 4. Results of MC simulations in a realistic scenario, with unknown mobile position and snapshot based RP initialization followed by MHT. Simulations here feature trajectories parallel to the wall. The red column shows whether the MHT was able to resolve initial ambiguities within simulation time. Performance values corresponding to specific RMSE quantiles are shown in green for the mobile estimation and in blue for the RP estimation. The illustrative bars are normalized per column. See Fig. 3 for a description of the different measurement configurations.

here for the same symmetry axis reasons, the RPs drift away from the wall.

Finally, looking at the combination of PDoA and Doppler measurements, we can see that using two aligned symmetry axes ($\theta_{\|\mathrm{u}}+v$ and $\theta_{\|}+v$) leaves the results of $\theta_{\|\mathrm{u}}$ and $\theta_{\|}$ almost unchanged, since the additional information gained from the Doppler measurement is very similar to the one of the $\phi = 0$ PDoA measurement, only with higher noise. Further we can see, that the combination $\theta_{\perp\mathrm{u}} + v$ does improve the values of both v and $\theta_{\perp\mathrm{u}}$ significantly. For the median values the improvement is minor compared to the best of the individual cases, but the improvement in the 95th percentile is significant, meaning that this configuration is a lot more robust and has significantly less MC runs where the RPs are drifting away. However, the same improvement cannot be observed for the case with the true measurement uncertainty, $\theta_{\perp} + v$, here the perpendicular case was very similar to the case without using Doppler, but for a parallel wall, the estimation performance degraded significantly compared to using Doppler only, i.e. v. The degradation can again be explained by the symmetry axis pointing toward the wall, which provides ambiguous and therefore imprecise information. The estimator then assigns too much confidence to this information, because the used measurement uncertainty value is effectively too small.

C. Quantitative evaluation of realistic scenarios

Whether the results from a simplified scenario also hold in a more realistic environment, is what we want to answer with the next results. Therefore we choose simulations, where the initialization of RPs has to happen based on a snapshot measurement followed by tracking and resolving initial ambiguities with an MHT. In this more realistic scenario we also assume the mobile track to be unknown, leading to not only a mapping, but a SLAM problem. In this scenario we focus on tracks parallel to the wall, since the RPs have to be tracked here over a longer distance. Further, since the mobile position has to be estimated, the choice of angular measurement configurations affects not only the MPC measurements as above, but also the LoS measurements.

The results of this second simulation set are shown in Fig. 4, where in contrast to Fig. 3 we have RMSE quantile values for the mobile. Additionally, the column “No conv.” indicates whether the initial ambiguities of the RP measurements was resolved during the simulation run. If the initial ambiguities were resolved, we speak of a converged MHT.

The cases $\theta_{\|\mathrm{u}}$, v, and their combinations show problems with converging during the simulation time for some MC runs. One possible explanation is that for straight trajectories, it is hard for the estimator to decide if the wall is above or below the measurements symmetry axis, especially when the estimator uses a low measurement noise. Furthermore, the measurements symmetry axis is aligned with the wall, which benefits estimating RP positions, but harms LoS measurements. The LoS propagation paths, between the mobile and the anchors, are in some time steps aligned with the measurements symmetry axis and therefore as discussed earlier the alignment leads to degraded LoS angular measurements. Especially in $\theta_{\|}$ and $\theta_{\|} + v$, where the estimator is even overconfident in the degraded angular LoS measurement, this alignment leads to many drift-offs of the mobile and thus an overall degraded estimation performance. The fact that these two scenarios converge more robustly compared to $\theta_{\|\mathrm{u}}$ and v can also be explained by this overconfidence, the MHT does converge, but either to a wrong solution, or after successful convergence, the tracking is unstable and the estimate starts to drift away.

Observing $\theta_{\perp\mathrm{u}}$ and $\theta_{\perp}$ in Fig. 4, we see that for the same overconfidence reason as in Fig. 3, the measurement with the more uncertain measurement noise value $\theta_{\perp\mathrm{u}}$ performs slightly better. As in the simplified case this improvement can be seen more dominant in the combined cases, $\theta_{\perp\mathrm{u}}+v$ performs significantly better than $\theta_{\perp}+v$. Interestingly, these combinations of two perpendicular symmetry axes, i.e. Doppler with symmetry axis along the wall and PDoA with one perpendicular to it, show no problems in filter convergence and is also less affected from frequent drift-offs. This can be explained, because most snapshot measurements are unambiguous, due to the perpendicular symmetry axes, which is ideal for initialization and supports also stable tracking.

In summary, the scenario with a combined measurement of two angular measurement functions with perpendicular symmetry axes performs best in the realistic scenario. The good performance is particularly pronounced when the higher effective noise in the PDoA measurement, whose symmetry axis points toward the wall, is considered in $\theta_{\perp \mathrm{u}}+v$, preventing overconfidence.

V. Conclusion

This work introduced a multipath-assisted localization and mapping approach that uses reflected signal components to jointly estimate the position of a moving receiver and the locations of RPs in the surrounding environment. Extending the work of [7], we focus on analyzing, comparing, and combining different sources of angular information from a two-antenna receiver array using PDoA and Doppler. Requiring only a simple ranging protocol with two antennas on the receiver makes this approach suitable for practical implementation with low-cost radio platforms, including UWB-based systems.

In simulations we demonstrated that RPs can be tracked using distance and either PDoA or Doppler measurements or both. The results showed that the orientation of the symmetry axis of the angular measurements, PDoA and Doppler, plays a major role in the estimation performance. For Doppler measurements, this symmetry axis is oriented along the mobile's velocity vector, if the Tx is static. In PDoA measurements this symmetry axis can be rotated by rotating the mounting angle of the antenna array. If the symmetry axis of the measurement is perpendicular to the propagation path, the estimator performance was significantly better than if they were aligned. Assuming a higher measurement noise could partly compensate for degraded measurements, when the propagation path and symmetry axis are aligned.

Next we analyzed more realistic scenarios, with realistic snapshot initialization, MHT and additional self localization of the mobile, i.e. SLAM. Here, we focused on trajectories parallel to the wall, since these cause the RPs to move farther along the wall and therefore increase the mapped wall area. The realistic scenarios showed a clear benefit of combined measurements with perpendicular symmetry axes. To be specific combining distance, Doppler and PDoA measurements with $\phi = \frac{\pi}{2}$. This measurement setup was most robust with respect to both stable tracking at challenging trajectories, that in other configurations led to drift-offs, and resolving initialization ambiguities quickly. The robustness was especially observable, if the estimator treated the PDoA measurement with symmetry axis pointing towards the RPs with an effectively higher noise value.

Compared with conventional VT-based approaches, which typically rely on static VT and simplified wall models, the proposed method estimates the physical RPs directly. Using RPs makes it suitable for scenarios in which autonomous systems encounter unknown or non-planar boundaries, such as caves, damaged buildings, or cluttered indoor environments.

Future work may focus on validating the method through experimental measurements and extending the simulations to more challenging scenarios with complex trajectories, richer multipath conditions, and more irregular wall shapes. The future developments could also include the development of a channel estimator that computes MPC distance, Doppler and PDoA measurements from raw antenna data. Further improvements could include more robust estimation strategies, e.g., an adaptive measurement-noise model that depends on the measured value and compensates for cases in which the measurement symmetry axis aligns with the propagation path.

References

[1] C. Cadena, L. Carlone, H. Carrillo, Y. Latif, D. Scaramuzza, J. Neira, I. Reid, and J. J. Leonard, "Past, present, and future of simultaneous localization and mapping: Toward the robust-perception age," *IEEE Transactions on Robotics*, vol. 32, no. 6, pp. 1309–1332, 2016.

[2] C. Gentner, T. Jost, W. Wang, S. Zhang, A. Dammann, and U.-C. Fiebig, "Multipath assisted positioning with simultaneous localization and mapping," *IEEE Transactions on Wireless Communications*, vol. 15, no. 9, pp. 6104–6117, 2016.

[3] E. Leitinger, F. Meyer, F. Hlawatsch, K. Witrisal, F. Tufvesson, and M. Z. Win, "A belief propagation algorithm for multipath-based SLAM," *IEEE Trans. Wireless Commun.*, vol. 18, no. 12, pp. 5613–5629, 2019.

[4] A. Zayets and E. Steinbach, "Interpolation and extrapolation of multipath fingerprints using virtual transmitter placement," in *2018 IEEE International Conference on Communications (ICC)*, 2018, pp. 1–7.

[5] H. Jung, S. Zhang, H. Park, and S. Kim, "From echoes to maps: Collaborative learning of unstructured spaces with multipaths and graph neural network," in *Int. Conf. Acoustics, Speech and Signal Processing (ICASSP)*, 2026, pp. 22 112–22 116.

[6] O. Kaltiokallio, E. Rastorgueva-Foi, J. Talvitie, Y. Ge, H. Wymeersch, and M. Valkama, "Robust snapshot radio SLAM," *IEEE Transactions on Vehicular Technology*, vol. 74, no. 5, pp. 8460–8465, 2025.

[7] B. J. Müller, M. Schmidhammer, M. Walter, C. Gentner, S. Zhang, and A. Dammann, "Multipath assisted positioning with arbitrary wall shapes using Doppler information," in *Int. Conf. Indoor Positioning and Indoor Navigation (IPIN)*, 2025, pp. 1–6.

[8] B. Chen, C. Marshall, and G. Dolmans, "Multipath-assisted simultaneous localization and mapping in single-anchor systems," in *Int. Conf. Indoor Positioning and Indoor Navigation (IPIN)*, 2025, pp. 1–6.

[9] H. Naseri and V. Koivunen, "Cooperative simultaneous localization and mapping by exploiting multipath propagation," *IEEE Transactions on Signal Processing*, vol. 65, no. 1, pp. 200–211, 2016.

[10] Y. Bar-Shalom, X. R. Li, and T. Kirubarajan, *Estimation with Applications to Tracking and Navigation*. Wiley-Interscience, 2001.

[11] H. L. V. Trees and K. L. Bell, *Bayesian bounds for parameter estimation and nonlinear filtering/tracking*. Wiley-IEEE press, 2007.

[12] J. Montiel and L. Montano, "Efficient validation of matching hypotheses using mahalanobis distance," *Engineering Applications of Artificial Intelligence*, vol. 11, no. 3, pp. 439–448, 1998.

[13] S. Blackman, "Multiple hypothesis tracking for multiple target tracking," *IEEE Aerospace and Electronic Systems Magazine*, vol. 19, no. 1, pp. 5–18, 2004.

[14] D. Reid, "An algorithm for tracking multiple targets," *IEEE Transactions on Automatic Control*, vol. 24, no. 6, pp. 843–854, 1979.

[15] M. Heydariaan, H. Dabirian, and O. Gnawali, "Anguloc: Concurrent angle of arrival estimation for indoor localization with uwb radios," in *Int. Conf. Distributed Computing in Sensor Systems (DCOSS)*, 2020, pp. 112–119.

[16] J. Krška, C. Gentner, and V. Navrátil, "Phase difference of arrival aided downlink time difference of arrival ultra-wide band positioning system," *IEEE Access*, vol. 13, pp. 81 628–81 642, 2025.

[17] A. Manikas, *Differential geometry in array processing*. Imperial College Press, 2004.